

New tailoring of photocatalyst for the photocatalytic CO₂ reduction

Zambaga Otgonbayar¹, Chang Sung Lim¹, Suresh Sagadevan², Kyung-Sang Cho³, Won-Chun Oh^{1*}

¹ Department of Advanced Materials Science & Engineering, Hanseo University, Chungnam 31962, South Korea

² Nanotechnology & Catalysis Research Centre, University of Malaya, Kuala Lumpur, Malaysia

³ Department of Cosmetics, Incheon Jaeneung University, Incheon 22573, South Korea

Abstract: The conversion of carbon dioxide into hydrocarbon fuels over photocatalyst is reasonable research topic. Specially, the manufacture of methanol is more advantageous than methane and carbon monoxide. The designing of the novel-structured catalyst is the main factor how the carbon dioxide converts into hydrocarbon fuels. The most importantly, effective charge transfer property is the main factor of a photocatalyst. Nowadays, 2D-structured graphene united ternary nanocomposite showed superior UV/visible light active, which had photo-redox catalyst owing to the enhanced quantum efficiency. This review paper mainly presents the influence of various factors on the photocatalytic performance, the type of photocatalyst and the reaction mechanism.

Keywords: Photocatalytic CO₂ reduction, Semiconductor, 2D graphene, Metal nanocomposite.

1. Introduction

The contamination of air is a considerable problem in the world. In the urban society, to provide an abundant energy and the most energy require fulfilled by the combustion of fossil fuel. Carbon dioxide (CO₂) is a kinetically and thermodynamically stable molecule, thus CO₂ conversion reactions are endothermic and need efficient catalysts to obtain high yield. Fossil fuel is one of the largest energy sources in the world and their continuously combustion is belonging to the primary producer of carbon dioxide in the atmosphere. For the past few decades, there has been an increased interest in the carbon mitigation plan. Especially, the process of photocatalytic CO₂ reduction into fuels can not only convert solar energy into stable chemical energy directly but also capture and utilize CO₂ in the atmosphere. It helps to alleviate global warming effects considering that CO₂ contributes mostly to the worldwide climate change. As a result, photocatalytic CO₂ reduction has been considered as one of the most promising ways to obtain clean energy supply due to the following advantages: solar energy utilization, chemical energy storage, and CO₂ capture. The process of conversion/reduction of carbon dioxide into

solar fuels divided into several methods. Among them, photocatalytic CO₂ reduction in aqueous media has sparked a huge interest because of reactants' availability, low cost, system simplicity, etc. However, the performance of this photocatalytic system is too sluggish to meet the efficiency requirement of industrial commercialization. In the last few decades, intensive investigations have been conducted to improve the efficiency of photocatalytic CO₂ reduction using water (H₂O) as the hole scavenger, ranging from the exploration of novel catalysts [1], [2], bandgap engineering [3], recombination inhibition [4], to system optimization [5], [6]. Photocatalytic reduction includes photo-generated charge carrier behaviors inside photocatalysts and surface reactions, so both of them should be considered in evaluating the STF efficiency. Especially for the photocatalytic CO₂ reduction in water, the gas adsorption is of the first concern during the complicated gas-liquid-solid reaction because the reaction kinetics is highly correlated with the surface gas concentration [7]. Furthermore, CO₂ reduction reactions are multi-electron transfer processes driven without sacrificial agents, leading to complicated pathways, and different product types. Nevertheless, an analysis of the whole photocatalytic reduction processes is still missing. Therefore, it is necessary to establish a comprehensive model for conducting the efficiency assessment of the water-based photocatalytic CO₂ reduction system.

The fundamental process of photocatalytic CO₂ reduction progressed using a semiconductor photocatalyst in aqueous condition. It includes the following steps: (1) light absorption, (2) charge separation, (3) charge carrier migration and recombination, (4) surface redox reaction [8]. For the first step, the photocatalyst absorbs photons with energies greater than its bandgap. In the second step, electrons are excited from the valence band to the conduction band by absorbed photons, generating electron-hole pairs. These charge carriers migrate from the bulk to the surface of the semiconductor photocatalyst in the third step, and the unpleasant issue of recombination will arise including radiative recombination and non-radiative recombination. In the last step, electron-hole pairs participate in the redox reaction on semiconductor surface reaction sites. The carrier recombination can be divided into the radiative recombination and the non-radiative recombination. On the non-equilibrium condition, the radiative recombination rate is proportional to the product of the electron concentration and the hole concentration [9], [10]. The surface redox reaction is crucial to the whole photocatalytic process. The determination of surface reaction rate is based on reaction product types and reaction mechanisms. There are a great variety of CO₂ reduction products including methanol (CH₃OH) [11], carbon monoxide (CO) [12], methane (CH₄) [13], and so forth. Among all products, CH₃OH is called the new fuel of the 21st century on account of its high energy density and high security and is used as raw material in chemical production widely [14]. Subsequently, CH₃OH is chosen as the reaction product. The reaction routine of CO₂ to CH₃OH is complicated, and there have been several reaction pathways proposed so far including the formaldehyde pathway, the carbene pathway, and the glyoxal pathway [15], [16], [17], [18].

From the charge carrier balance equation, there are three factors mainly affecting the STF efficiency - the semiconductor bandgap, the recombination coefficient, and the

gas coverage ratio of photocatalyst surface. The semiconductor bandgap directly limits the light absorption of photocatalyst. The recombination coefficient represents the degree of charge carrier recombination. The gas coverage ratio reflects the performance of the reactant absorption and desorption. Without loss of generality, the intrinsic semiconductor CdSe is chosen as an example to analyze the reduction of CO₂ to CH₃OH. In the particulate photocatalytic system, the solubility of CO₂ in water remains low ($H^{\circ}0.034$ M at 1 bar and 300 K [19]), which limits the gas partial pressure in aqueous solution. Meanwhile, the reactant adsorption and desorption processes are also difficult [20, 21, 22]. Furthermore, the combination of metal / metal oxide with graphene by increasing the efficiency of the semiconductor is a very reliable method. Graphene is a 2D structured sp²-hybridized carbon material in a honeycomb structured. Graphene has many profitable properties, such as mechanical strength [45], molecular barrier ability. In addition, the preparation procedure of graphene has categorized in two groups: (i) top to down method-synthesized by etching out crystal planes (mechanical exfoliation, oxidation-reduction, liquid phase exfoliation), (ii) bottom to up method-synthesized by the atoms stick onto the substrates which gives rise to crystal planes (chemical vapor deposition, epitaxial growth). There are four routes for synthesis of graphene which include those of Brodie, Staudenmaier, Hofmann and Hummers. Currently, the Hummers method is widely used as it is a fast and safety method. Carbon materials combined with semiconductor, which including a graphite, carbon black, activated carbon, carbon fibers, carbon nanotubes (CNTs), and fullerenes. Furthermore, the unique two-dimensional planar structure and high specific surface of GR mean that it shows great potential as a carrier and multifunctional material for transferring electrons and holes. The mechanism of enhancement of photocatalysis by Graphene: semiconductors possess a low-energy VB which has a full of electrons, a high-energy CB which has an empty orbital and has a bandgap difference between two band state.

2. Experimental part

The mechanisms of photocatalysts prepared by surfactants are complex and It is generally believed that due to the non-covalent interactions, such as hydrogen bonding, π - π interaction, and van der Waals interaction, between the surfactant and solid material, the surfactant was adsorbed on the surface of the solid material, inducing the material to self-assemble. Surfactant-assisted photocatalysts have been synthesized through various techniques, which mainly include sol-gel method, hydrothermal method, solvothermal method, emulsion method, and sonochemical method, etc. Among them, the most common synthesis methods are the sol-gel method, hydrothermal method, and solvothermal method. The sol-gel and hydrothermal methods are used in an aqueous media, whereas the solvothermal employs a non-aqueous media for the reaction.

2.1. Sol-gel method

The sol-gel method has the advantages of high stability, short soaking times, low reaction temperature and high purity of products, and it is considered to be one of the most

promising methods for synthetic photocatalysts. In addition, the photocatalysts particles prepared by the sol-gel process generally have a narrow and uniform distribution and thermal stability. Therefore, the sol-gel method has attracted much attention in the preparation of porous photocatalysts [23]. This approach has been successful in the controllable design of multi-dimensional photocatalysts, such as pellets, fibers, films, and blocks. The chemical reactions involved in the sol-gel process are based on inorganic polymerization. As shown in Figure 1, the preparation process of the method is divided into three steps, namely hydrolysis, polymerization and gel drying [24].

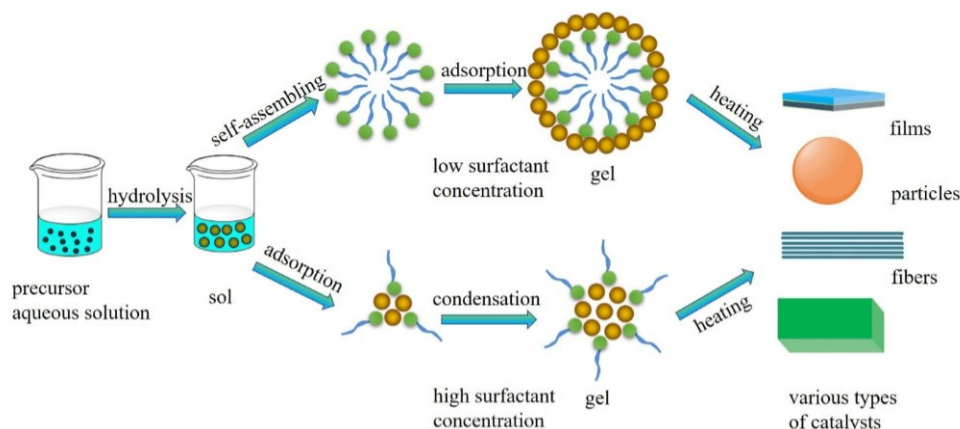


Figure 1. The possible preparation process of surfactant-assisted photocatalysts by sol-gel method [24].

Firstly, a solution of the precursor molecules needs to be hydrolyzed. The precursor is typically a metal organic compound such as an alkoxide, a chelated alkoxide or a metal salt. After hydrolysis, a suspension of colloidal particles (sol) is formed. Secondly, a large amount of water is present in the sol, and during the gelation process, the system loses fluidity and forms an open skeleton structure (gel). Finally, the gel is calcined to remove the surfactant to obtain the final photocatalyst [25], [26].

2.2. Hydrothermal method

Compared with other crystal preparation methods, the photocatalysts prepared by the hydrothermal method have the advantages of good grain development, small particle size, uniform distribution, and low-cost raw photocatalysts. In particular, they have the unique advantages of high crystallinity and morphology control [26]. The hydrothermal method has been successful in the controllable design of multi-dimensional photocatalysts, such as 1D photocatalysts (nanowires, nanobelts, nanotubes), hollow and thin films.

In general, the hydrothermal method uses water as a solvent, and the sample needs to be dissolved and recrystallized firstly [27]. The possible preparation process of the hollow structure is shown in Figure 2. The sample is mixed in a solution and the reaction is carried out at a certain temperature [28]. During the period, due to the presence of the surfactant, the samples self-assemble to form fine particles, and as the crystal grains grow up, the final morphology products are obtained.

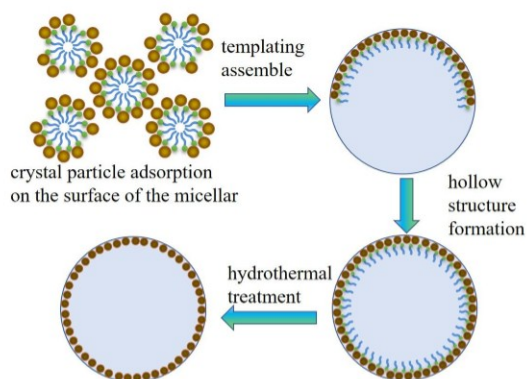


Figure 2. The possible preparation process of hollow photocatalysts by hydrothermal method [28].

2.3. Solvothermal method

The solvothermal method is developed on the basis of the hydrothermal method, using an organic or non-aqueous solvent as a solvent and the mixture reacting at a certain temperature [29], [30]. The hydrothermal method is commonly used to the preparation of oxide photocatalysts or some water-insensitive sulfur-containing compounds, while the preparation of some water-sensitive compounds such as III-V semiconductors, carbides, fluorides, and other photocatalysts are not applicable. Compared with the hydrothermal method, the solvothermal method uses a non-aqueous solvent, which expands the range of solvent-based raw materials [31].

It is worth noting that, unlike the sol-gel and hydrothermal methods, the process of solvothermal preparation of photocatalysts is mainly divided into nucleation, dissolution, recrystallization, and growth, as shown in Figure 3 [32].

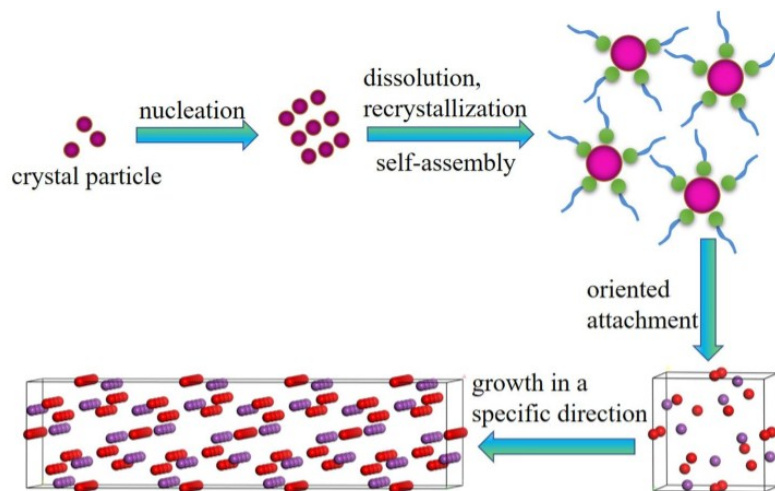


Figure 3. The possible preparation process of surfactant-assisted photocatalysts by solvothermal method [32].

2.4. Sonochemical method

The sonochemical method is a method of accelerating chemical reactions using ultrasonic waves. The sonochemical reaction is mainly caused by acoustic cavitation – the formation, oscillation, growth, shrinkage, and collapse of liquid hollow bubbles. This method has become an important tool for the production of novel nano-sized materials under ambient conditions in synthetic chemistry [33]. Compared with the sol-gel method, hydrothermal method, solvothermal, etc., the sonochemical method has the advantages that the reaction temperature is low, and the high temperature is not required. According to the hotspot theory, local hot spots can reach extremely high temperatures (>5000K) when bubbles burst, and these extreme conditions can be used to synthesize a variety of materials. The mechanism of the sonochemical method is relatively complicated. It is generally believed that water decomposes into hydroxyl radicals and hydrogen under the action of ultrasonic waves, thereby triggering a series of chemical reactions.

2.5. Emulsion method

The emulsion polymerization method is a method in which a monomer is dispersed in water by an emulsifier and mechanical stirring to form an emulsion, and an initiator is added to initiate polymerization of the monomer. The emulsion polymerization has the characteristics of high polymerization speed, high reaction conversion rate, low viscosity, stable dispersion system, and easy control. However, the separation and precipitation process of the polymer obtained by the emulsion polymerization method is complicated, and a demulsifier or a coagulant is added so that there are many residual impurities in the product [34, 35]. The polymerization mechanism can be divided into four stages: dispersion stage, aggregation stage, growth stage, and polymerization completion stage. The possible synthesis process of the emulsion polymerization process is shown in Figure 4.

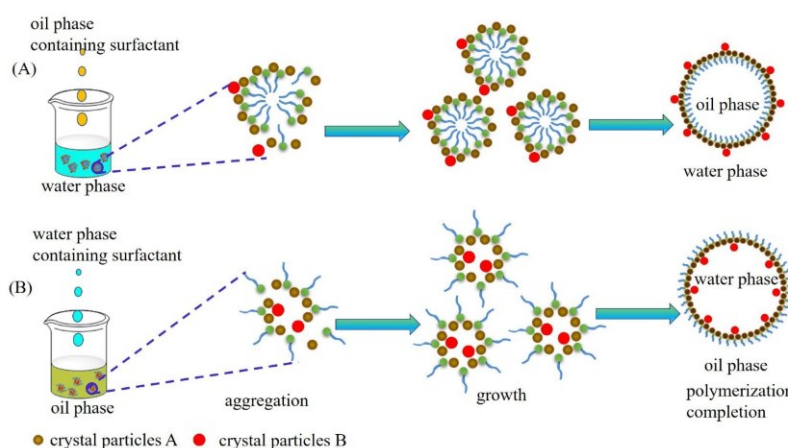


Figure 4. The possible preparation process of surfactant-assisted photocatalysts by emulsion (A) water-in-oil, (B) oil-in-water polymerization method [35].

2.6. Pechini method

The Pechini method has been widely used in the synthesis of oxide nanocrystals. The method is based on an intensive blending of positive ions in a solution, controlled transformation of the solution into a polymer gel, removal of the polymer matrix and development of an oxide precursor with a high degree of homogeneity. When compared to other methods, the Pechini method has better compositional homogeneity, lower toxicity and lower cost [36].

The Pechini method stands out among several chemical synthesis methods because it allows for the use of different temperatures and proportions of citric acid and metallic cations, enabling controlled particle and/or agglomerate stoichiometry and morphology, compositional homogeneity, and low toxicity to produce a monophasic nanometric powder [37]. In the Pechini method the reaction is hydrolytic and produces a polymer which, after calcination, forms an oxide. The Pechini process involves two basic chemical reactions: the formation of a chelate complex consisting of carboxylic acid, chelating agent, and metallic matrix, followed by its polyesterification with an excess of polyalcohol (as shown in Figure 5). The reactants usually employed in this application are citric acid and glycol ethylene.

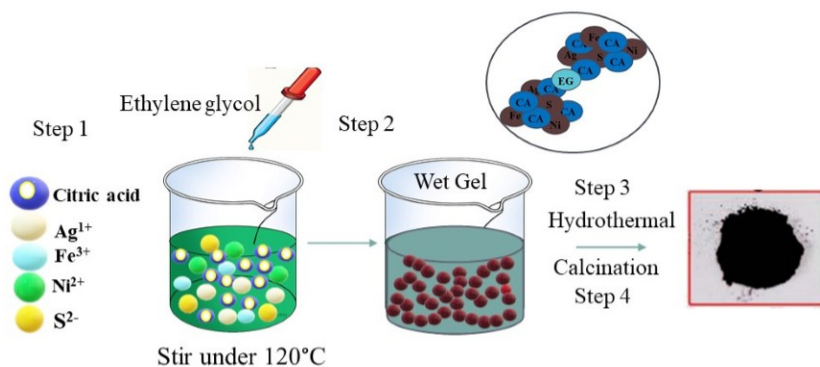


Figure 5. The possible preparation process of Pechini method [35].

2.7. Experimental part of Photocatalytic CO₂ reduction

The photocatalytic CO₂ reduction in aqueous media has sparked a huge interest because of reactants' availability, low cost, system simplicity, etc. However, the performance of this photocatalytic system is too sluggish to meet the efficiency requirement of industrial commercialization. In the reduction of CO₂, the water used as a hole scavenger, ranging from the exploration of novel catalysts [1], [2], bandgap engineering [3], recombination inhibition [4], to system optimization. In detail, a photocatalytic reduction of CO₂ was examined in a three-part reactor (Figure 6), using the 500-W metal halide lamp as the light source. In detail, 100 mg of the photocatalyst with two different sacrificial scavengers were dispersed into 0.04 M NaHCO₃ containing 50 ml solvent and stirred it

for 1 h, filled the reactor with pure CO₂ gas for 30 min, and turned on the light. After 48h of reaction, we withdrew the different amounts of final samples using a syringe and membrane filter, which were 0.45 μm in pore size and 47 mm in diameter, respectively, from the reactor every 12 h. The final samples evaluated by a “Quantitative analysis of alcohol” method. In alcohol analysis, 10 ml of 0.1 M CrO₃ added into 1-ml sample and agitated it for 15 min, then centrifuged the suspension (10.000 ppm/15 min). The concentration of acquired solution examined by a UV spectrophotometer (Optizen POP, Korea) using a quartz cell (1 cm × 4.5 cm) [40].

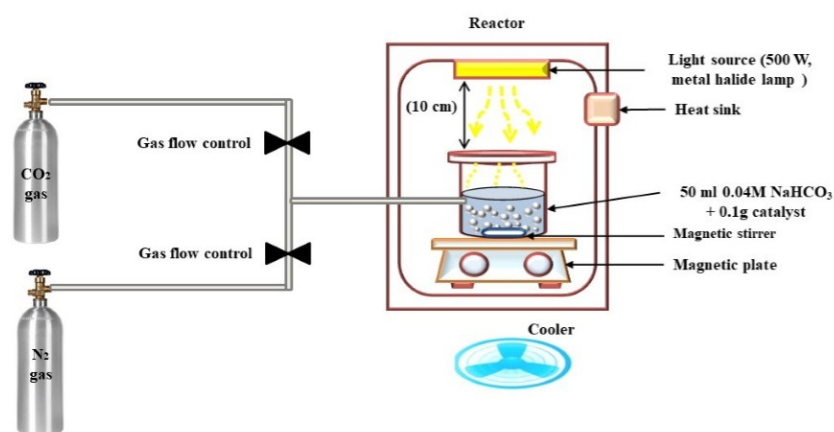


Figure 6. Schematic diagram of the device of photocatalytic CO₂ reduction under the light irradiation [40].

3. Result and discussion

3.1. Characterization of photocatalyst material

The morphology structure, surface state and crystal characteristics of the samples were analyzed via TEM and HRTEM. Figure 7 shows the schematically illustrates the synthetic procedure for Pt-NGO-RT photocatalyst and TEM images. HR-TEM was performed to investigate the structural evolution and formation of Pt-NGO-RT hybrid photocatalyst (Figure 7 **b-g**). RT NPs exhibit a well-defined crystalline morphology of TiO₂ without any aggregation, as shown in Figure 7b. The disordered surface layer with a thickness of H'' 1-2 nm is formed on RT, confirming surface defects (Figure 7c). These surface defects could be due to the presence of Ti³⁺ sites resulting from hydrogen incorporation/oxygen vacancies [38]. HR-TEM images of the NGO-RT sample shows that RT NPs are anchored into the NGO sheet (Figure 7**d-g**), in which NGO layers are distributed over the RT surface, thus, offering a large surface area. In HR-TEM of Pt_{1.0%}-NGO-RT composite, Pt NPs are found to be uniformly distributed over the NGO-RT sample (Figure 7**f-g**), and EDS mapping reveals such distribution along with the presence of Ti, C, O, N, and Pt elements. Utmost Pt NPs can be observed on the RT surface, which forms the interface of Pt-RT. In XRD patterns, all the peaks correspond to anatase and rutile TiO₂, as shown in Figure 2a. GO's introduction did not alter the crystal phase of

P25 (TiO₂), where typical GO peaks were absent due to its lesser concentration and low diffraction intensity [39]. The FT-IR was applied to analyze to confirm the chemical interaction between NGO and RT. In the FT-IR spectra of NGO-RT and Pt_{1.0%}-NGO-RT samples, the 400-800 cm⁻¹ region's broad peak corresponds to Ti-O-C stretching [40] due to the interaction between RT (TiO₂) and NGO, which is absent in P25 and RT samples, see Figure 2d. Moreover, bands at <1200 and <1570 cm⁻¹ can be attributed to the C-N and C=C/C=N bonding in both NGO-RT and Pt_{1.0%}-NGO-RT portent successful doping of N into the GO matrix [41], [42].

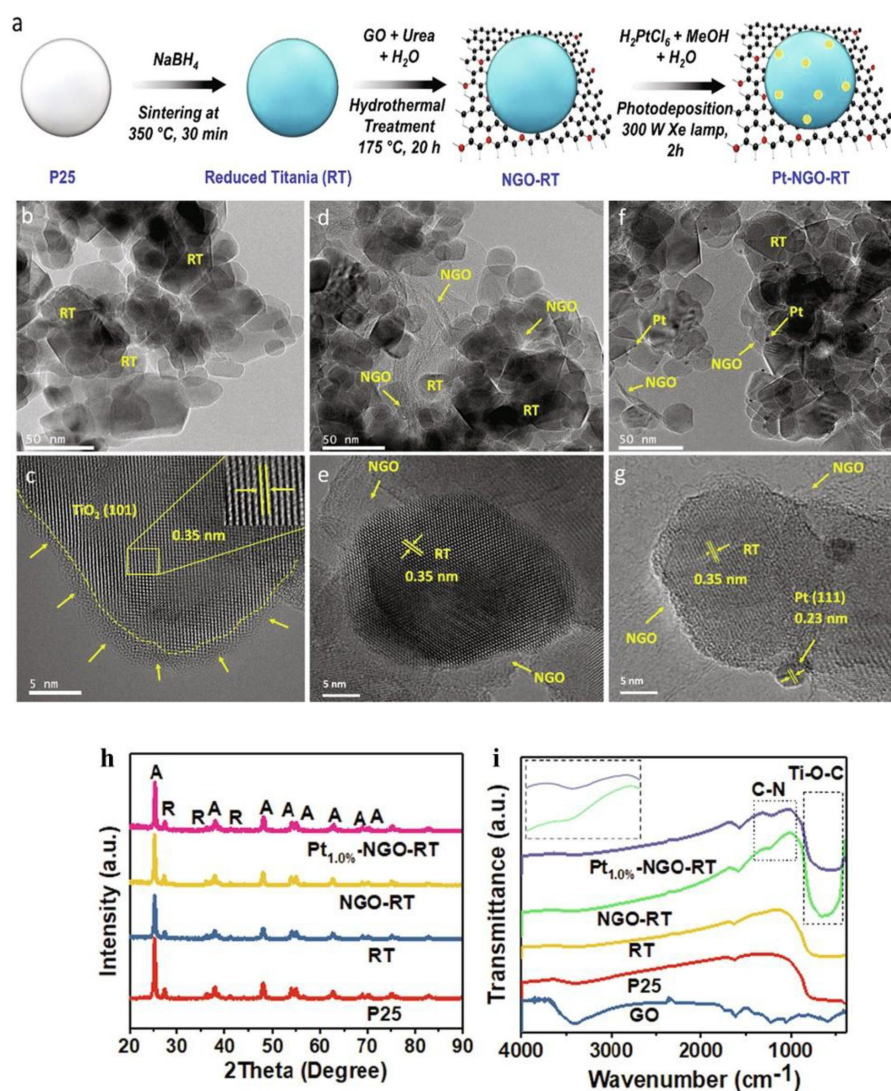


Figure 7. (a) Schematic illustration showing the synthesis of Pt deposited NGO-RT composite (Pt-NGO-RT), and the HR-TEM images showing the stepwise formation of Pt-NGO-RT; (a-b) RT, (c-d) NGO-RT, and (e-f) Pt_{1.0%}-NGO-RT samples, (h-i) XRD pattern and FTIR spectra [39, 40].

In this part, the morphologies and crystal characteristics of TiO_2 and 5.0RGO- TiO_2 catalysts were revealed by TEM and HRTEM (Figure 8). Figure 8d shows that the TiO_2 nanoparticles were embedded in the sheets of RGO. The thickness of the monolayer of the RGO was calculated to be 0.35nm. The calculated average particle size gradually decreased from *ca.* 11.44nm in TiO_2 to 11.39, 10.83, 10.46 and 9.38nm in 1.0RGO- TiO_2 , 2.0RGO- TiO_2 , 5.0RGO- TiO_2 and 10.0RGO- TiO_2 , respectively (Figure 8a and b). The addition of RGO, which served as the support, ensured more dispersion and suppressed the further growth of TiO_2 nanoparticles [43]. The d-spacing of 0.342/nm were consistent with anatase (101) plane of TiO_2 in both samples (Figure 8b and d), suggesting that RGO had little influence on the crystal phase of TiO_2 . The XRD patterns of the prepared RGO and RGO- TiO_2 catalysts are shown in Figure 8d. The peaks at $2\theta / = 25.9^\circ$ and 43.2° were assigned to planes (002) and (100) of the RGO sample. All other catalysts, including TiO_2 and RGO- TiO_2 , depicted similar XRD peaks, which agree well with the tetragonal anatase TiO_2 (JCPDS 21-1272). Since no characteristic peak of RGO was observed, there was no noticeable difference in the peaks of TiO_2 as the loading amount of RGO increases in the RGO- TiO_2 composite. It was reasoned that peaks of TiO_2 overlapped the peaks of RGO. Notably, from Figure 8 c (inset), the width of the major peak (101) in TiO_2 was widened with the increasing amount of RGO in RGO- TiO_2 composites. This widening changed the crystallite size of TiO_2 in the nanocomposites [44].

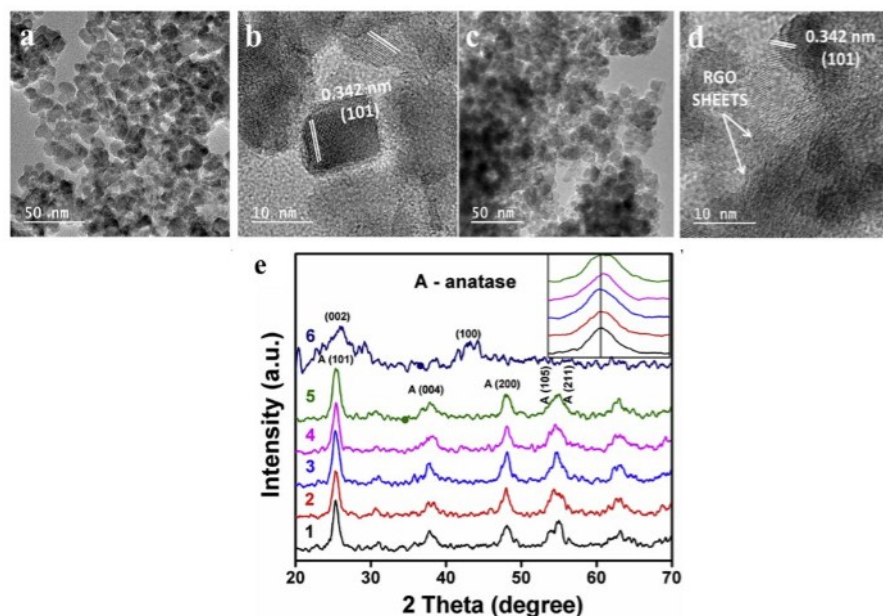


Figure 8. (a) TEM image of pure TiO_2 , (b) HRTEM of pure TiO_2 , (c) TEM image of 5.0RGO- TiO_2 , (d) HRTEM of 5.0RGO- TiO_2 , (e) XRD pattern of photocatalytic [43].

UV-Vis-DRS and PL spectra were used to investigate the optical properties of as-synthesized photocatalysts. As shown in 9a, compared to pristine P25, the RT exhibits a highly enhanced photo-absorption in the solar spectrum that can be attributed to the

formation of midgap states and surface disorders [45], which is consistent with XPS and EPR analysis. The light absorption of the NGO-RT sample further improved in the visible region due to $n-\pi^*$ transition. The Pt deposited samples showed noticeable enhancement in visible light assigned to the localized surface plasmon resonance (LSPR)[46]. The bandgap energies of photocatalysts were investigated by Tauc's plot, as shown in Figure 9b; the decreased bandgap in RT suggests the extended light absorption in the visible region due to the formation of mid-gap states. The narrowing bandgap energies in NGO-RT and Pt_{y%}-NGO-RT samples could be due to the construction of the Ti-O-C chemical bond between TiO₂ and NGO [47]. The decreased bandgap results in superior interfacial charge transfer among the Pt-NGO-RT composite, further strengthened by photoluminescence (PL) analysis, as shown in Figure 9c. Apparent quenching in PL intensity from P25 to Pt_{y%}-NGO-RT samples was due to the successful migration of charge carriers through the interface [48]. The decreased PL intensity also implies the active injection of a photogenerated electron from RT to NGO, and Pt NPs surfaces before the charge recombination [49]. These results demonstrate that the lower recombination of electron-hole in Pt-NGO-RT would accelerate the CO₂ reduction process. In the case of the absorption edge of TiO₂, which was determined by the extrapolation of the linear part of the plot to the absorption background in the visible light, was found to be around 392 nm, which did not change significantly in RGO-TiO₂ composites. The introduction of RGO into TiO₂ did not significantly cause a red shift to a longer wavelength in the absorption edge of TiO₂, and this phenomenon is discussed and further confirmed in the section devoted to the results of the theoretical study, as shown in Figure 9 d, e. The optical band gap energies of the prepared catalysts were also determined from the Tauc's plot of $[F(R)hv]^{1/2}$ versus the photon energy *via* the intercept of the tangent to the x-axis [50]. The band gap of TiO₂ was found to be 3.2eV, which gradually decreased to about 2.9/ eV with 10.0RGO-TiO₂. The observed decrease in the TiO₂ band gap was small and may be due to the formation of Ti-O-C bonds in the composite. From the X-ray diffraction (XRD) patterns in Figure 10 c, we found that all of identical peaks of the CABB@C₃N₄-10 % and CABB@C₃N₄-82 % samples can be well matched with a cubic double perovskite structure. As shown in Figure 10d, the absorption edge of the CABB@C₃N₄-82 % photocatalyst gives an apparent red shift compared with pure CABB and g-C₃N₄. Figure 10e displays the surface photovoltage (SPV) spectra of g-C₃N₄, CABB, CABB@C₃N₄-10 % and CABB@C₃N₄-82 %. Pure CABB and g-C₃N₄ exhibits a large negative signal and a weak positive signal of SPV, respectively. In the case of CABB@C₃N₄-10 %, the photogenerated electron transfers from g-C₃N₄ to CABB due to the formation of a type II heterojunction; thus, the SPS signal is negative, which is similar to the signal of CABB. A weak light adsorption from g-C₃N₄ (positive signal) and strong light absorption from CABB (negative signal) lead to the decreased signal of CABB. In the case of CABB@C₃N₄-82 %, the formation of Z-scheme species results in more electrons being kept at the g-C₃N₄; thus, the SPS signal turns positive compared with type II heterojunction, which is similar to the case for pure g-C₃N₄. Finally, transient photocurrent tests show that the CABB@C₃N₄-10 % and CABB@C₃N₄-82 % photocatalysts give a significant enhancement of photocurrent density compared to the pure CABB and the pure g-C₃N₄ (Figure 10g), also confirming

the higher charge separation efficiency. Interestingly, the intensity of photocurrent in CABB@C₃N₄-10 % is about 2 times higher compared with that in CABB@C₃N₄-82 %.

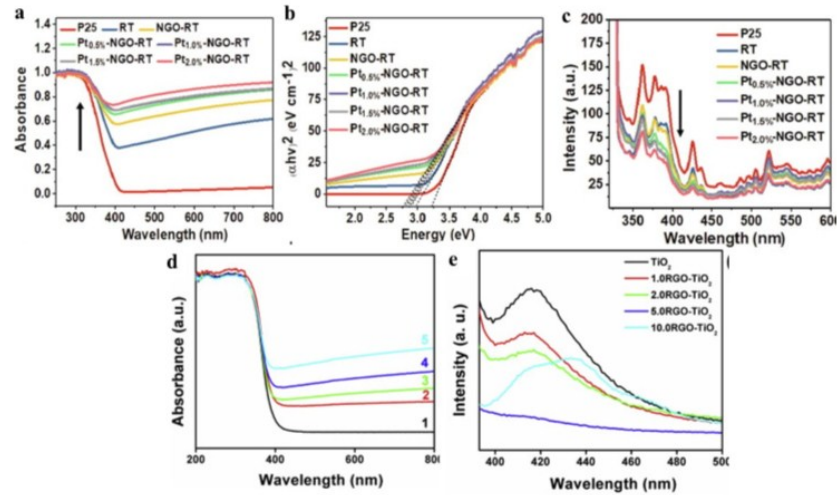


Figure 9. UV-Vis Diffuse reflectance spectra, Photoluminescence spectra of P25, RT, NGO-RT, and Pt_{y%}-NGO-RT samples, pure TiO₂ and RGO-TiO₂ composites [45, 50].

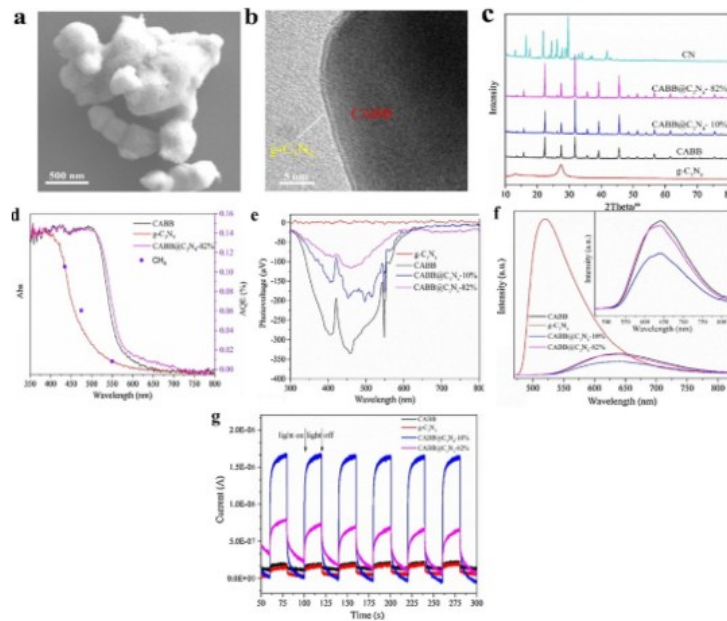


Figure 10. (a) SEM image of CABB@C₃N₄-82 %. (b) HRTEM image of CABB@C₃N₄-82 %. (c) XRD pattern of CN small pieces, g-C₃N₄, CABB, CABB@C₃N₄-10 % and CABB@C₃N₄-82 %. (d) Diffuse reflectance absorption spectra of g-C₃N₄, CABB, CABB@C₃N₄-82 % and Photocatalytic activities under monochromatic beams (at 4350475 and 550 nm) by CABB@C₃N₄-82 %. (e) Surface photovoltage spectra of CABB, CABB@C₃N₄-10 % prepared in toluene and CABB@C₃N₄-82 % prepared in dichloromethane solvent system. (f) Steady-state PL spectra of g-C₃N₄, CABB, CABB@C₃N₄-10 % and CABB@C₃N₄-82 % with an excitation wavelength of 435 nm. (g) Transient photocurrents of g-C₃N₄, CABB, CABB@C₃N₄-10 % and CABB@C₃N₄-82 % [48].

3.2. Photocatalytic performance and evolution of CO₂

The photocatalytic activity of the prepared series of catalysts RGO-TiO₂ was assessed for the reduction of CO₂ under UVA light for 16h with 5mg and benchmarked against TiO₂ using the same experimental conditions. In Figure 11 a, all prepared catalysts showed considerable activity for selective photocatalytic CO₂ reduction to methanol in water: ACN medium (16:2 v/v in mL) using TEOA (2mL) as the sacrificial electron donor. Measurements were conducted initially for the 8h at 4h intervals for the first day; then the reaction was stopped, stored in the dark for few hours and resumed almost midnight and allowed to run overnight for the next 8h till 16h (next day). For all samples, the production of methanol increased with time. TiO₂, as the control sample, exhibited a methanol production rate of *ca.* 1.95mmol g⁻¹ h⁻¹; this rate was lower than for all RGO-containing samples. The explanation of this observation could be that the large band gap and fast recombination of e⁻ - h⁺ pairs in TiO₂ [51,52]. The wrapping of RGO on TiO₂ exhibited a significant influence on the photocatalytic activity. Factors such as: (1) synergistic effect between TiO₂ and RGO as a result of hydrothermal reaction, which allows the formation of chemical bond [53, 54] and reduced recombination of e⁻ h⁺ pair [55], and (2) higher surface area which provides more active adsorption sites, and photocatalytic reaction centers [56]. Increase in photocatalytic activity was observed with a higher dosage of RGO from 1% to 5% weight ratio in the RGO-TiO₂ composites. However, a decreasing trend was found with the further addition of RGO, suggesting that excess RGO might work as a competitor with TiO₂. An excess amount of RGO could increase the unproductive consumption of photons in the photocatalytic system, thus shielding the light reaching the surface of the TiO₂ photocatalysts [57]. Hence, it was critical to get the optimum loading amount of RGO in the RGO-TiO₂ composites. Here, 5% RGO was the optimum as in 5.0RGO-TiO₂ with the methanol production rate of 3.41mmol g⁻¹ h⁻¹, almost double the pure TiO₂. Figure 11b reveals that all the composites were photocatalytically active under visible light with 2.0RGO-TiO₂ and 5.0RGO-TiO₂ performed almost equally, with the methanol production rate of *ca.* 2.33mmol g⁻¹ h⁻¹. However, as expected, TiO₂ showed little activity under visible light. These results suggest that RGO acted as a sensitizer for TiO₂ in a way to enhance its visible light activity. Hence, the reaction rate was mainly determined by the amount of TiO₂ catalyst present [58]. To check whether pure RGO alone was active for CO₂ reduction under UV and visible light, the equivalent weight of its calcined form was used. At similar conditions, it was observed that 13.48 and 31.61 μmol g⁻¹ h⁻¹ of methanol were produced. These values were so insignificant in comparison to ones obtained with bare TiO₂ and RGO-TiO₂ nanocomposites. The influence of reaction medium on the photocatalytic reduction of CO₂ was performed with 5.0RGO-TiO₂ in the presence of DMF, ACN, and DMSO by keeping other parameters constant under the visible light, as shown in Figure 11c. The trend in the photoreduction activity was found to be ACN > DMSO > DMF yielding 2.33, 0.95 and 0.74mmol g⁻¹ h⁻¹, respectively. CO₂ has a higher solubility in ACN medium, and this might play a crucial role in product formation. The photocatalytic activities of all the reported work on the use of graphene-TiO₂ composite for CO₂ reduction were measured in the presence of CO₂ and water vapor. Photocatalytic CO₂ conversion to hydrocarbon is challenging due to the high dissociation energy of the C=O bond (<750 kJ mol⁻¹) [59]. In addition, the CO₂ reduction process is closely related to the catalyst's band structure and electron-hole transportation. The absence of CO and H₂ in

the photocatalytic system suggests that the CO_2 reduction proceeds by the electron transfer process coupled with protons [60]. It requires eight electrons and protons at an E° redox potential above -0.24 eV ($E^\circ = -0.24 \text{ V}$ vs. NHE) to form CH_4 . The defect-induced RT can generate electron-hole pairs at the respective CB and VB suitable for the CO_2 reduction to CH_4 . Pt NPs deposited on NGO-RT further restricts the unwanted charge recombination due to the formation of a Schottky junction between RT and Pt NPs and improves the catalytic activity, as shown in Figure 11 (d, e). Hence, the rapid charge electrons transformation in Pt-NGO-RT leads to improved catalytic activity and stability. Noteworthy, the continuous formation of CH_4 over 7 h was due to continuous adsorption and conversion of the $\text{CO}_2/\text{H}_2\text{O}$ into CH_4 on the surface of Pt-NGO-RT, as shown in Figure 11 (f, g). Therefore, spatial separation and photoexcited electron/hole transfer give rise to improved photocatalytic CO_2 reduction towards the selective formation of CH_4 .

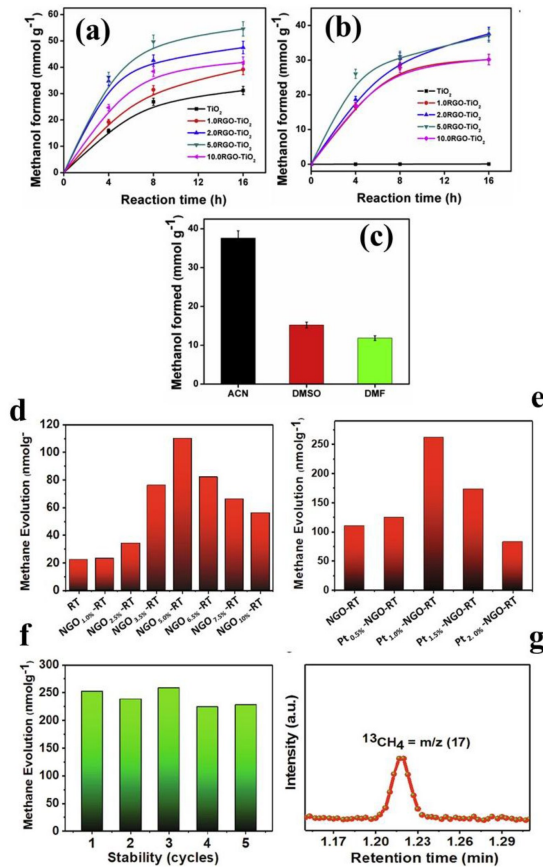


Figure 11. a) Rate of the formation of methanol from the reduction of CO_2 under UVA light irradiation, (b) rate of the production of methanol from the reduction of CO_2 under visible light irradiation, (c) influence of the reaction medium for the production of methanol from CO_2 reduction under visible light by 5.0RGO-TiO₂ for a period of 16/ h, (d-e) Methane evolution under light irradiation with TiO₂ and other TiO₂ united nanocomposite, f) Stability and reusability test of photocatalyst within 5 cycles, g) Mass spectrum of methanol [51, 52].

The process parameters used in the CO₂ reduction influence the product selectivity. Formation of products like CH₃OH, C₂H₅OH, and formaldehyde are possible, but the probability is high in the aqueous environment [61]. The aqueous phase selectivity also relies on the catalysts along with other considerations, such as sacrificial agents, solution pH, etc.[62]. However, product selectivity in the gas-phase mainly depends upon the catalysts used for CO₂ reduction. Our catalytic system is gas-phase; the possibility of H₂, CO, CH₄, and C₂H₆ product formation is more viable. In our experiments, CH₄ was the main product obtained with an insignificant quantity of C₂H₆. Figure 12 a, b shows the chromatograph result of CO and H₂ evolution for Pt_{1.0%}-NGO-RT sample, where no peaks related to CO or H₂ are present. Moreover, the gas-phase reaction system conquers the H₂ evolution and increase the leeway for CH₄ formation [63]. However, similar types of catalysts have been reported for CH₃OH evolution using sacrificial agents in the aqueous system.

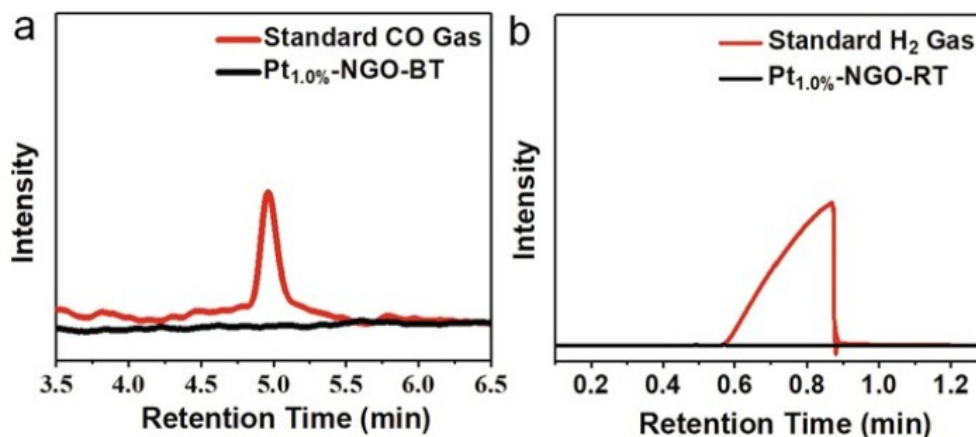


Figure 12. TCD chromatogram of (a) CO and (b) H₂ in Pt_{1.0%}-NGO-RT sample [62].

Figure 13 (a) shows the recyclability and reusability test of the photocatalyst for the CO₂ reduction under the light irradiation. According from this test, there is no obvious difference of the reduction performance observed after 12h test, which totally 4 recycle. After recycle test, we analyzed the crystal structure of the photocatalyst via XRD. The XRD pattern confirmed that there is no significant change for the crystal structure of the photocatalyst [64]. Figure 13 (c, d) shows the FTIR and PL spectra. The photocatalytic activity was estimated towards CH₄ formation, where intermediate CH₃[•] (methane radical) generated over the catalytic surface eventually reacts with H⁺ to form CH₄. In the FTIR spectra of the used sample, two peaks at 2853.7 and 2915.7 cm⁻¹ correspond to the C-H stretching band attributed to the CH₃[•] intermediate present over the catalyst. In PL spectra, Pt_{1.0%}-NGO-RT exhibit broad luminescence spectra excited at 330 nm, while such peak is absent in pristine. This means the valence band of catalysts lies below the water oxidation potential to produce OH[•]/OH⁻.

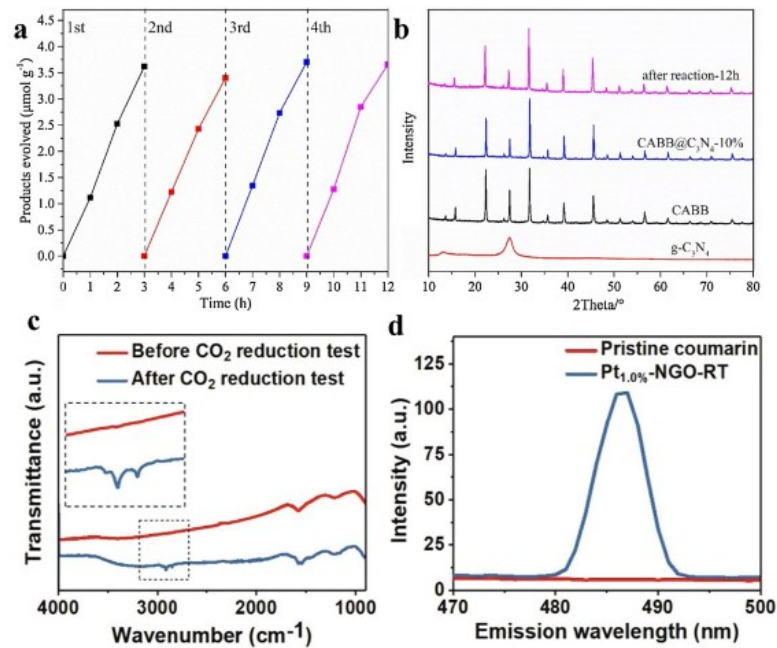


Figure 13. (a) Recyclability test of CABB@C₃N₄-10 %. (b) XRD pattern of photocatalyst after recycling test. (c) Mechanistic study on the mechanism with (a) FTIR spectra of CH₃• radical detection and (b) PL spectra of Hydroxyl (OH•) radical [64].

Figure 14 shows the schematic illustration of the photocatalyst, band energy diagram and reduction of CO₂ into methanol and methane under the surface of photocatalyst. Figure 14 (a, b) shows the theoretical mechanism of CO₂ photoreduction which using RGO-TiO₂. Under UV light photoexcitation, electrons and holes are produced in TiO₂ nanoparticles, and electrons are transferred into RGO. Under visible light photoexcitation, charge transfer results in holes in TiO₂ and electrons in RGO. The positive effect of the presence of graphene on the reduction of CO₂ is associated with a high electrocatalytic activity of carbon electrodes in reduction reactions [65]. Figure 14 c shows the bandgap diagram and reduction of CO₂ under the surface of Pt-NGO-RT composite under the light irradiation. Bandgap value of each nanocomposite was analyzed via Tauc's plot. The energy difference of 0.53 eV in the work function of pristine RT (5.01 eV) and NGO-RT (5.54 eV) suggests the downward band bending of RT at the interface of NGO-RT composite. The resulting downward band bending facilitates the interfacial electron transfer from the CB of RT to the NGO and decreases the electron-hole recombination. In the photocatalytic process, CO₂ molecules probably adsorb on amorphous RT and the N-site of NGO. The amount of CH₄ evolution in RT is relatively low, suggesting the probability of a lower amount of CO₂ adsorption on RT and more on the NGO's surface [66]. It has been reported that N-doped graphene has great potential for CO₂ capture due to the formation of a hydrogen bond between the N functionality and CO₂ molecule [67].

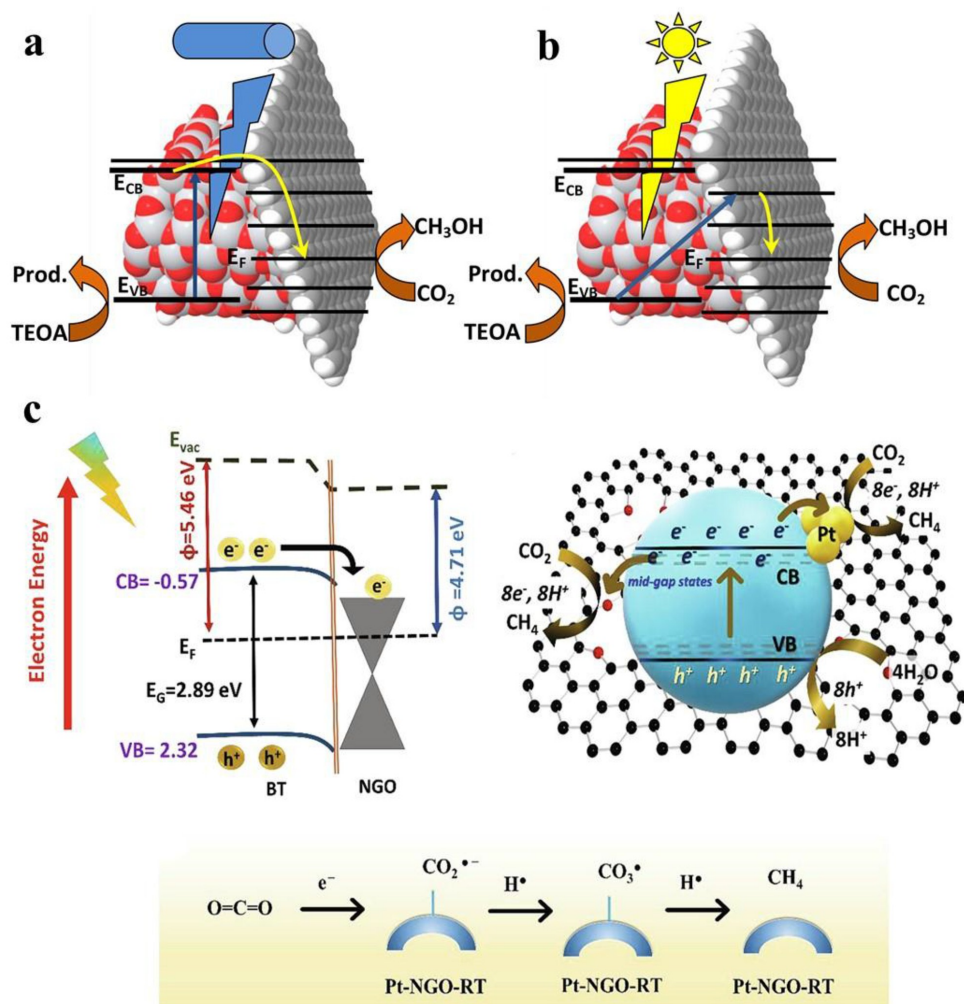


Figure 14. Schematic illustration of the electron transfer process in the graphene-anatase structured photocatalyst and energy band diagram of the Pt-NGO-RT composite and reduction of CO₂ into methanol and methane on the surface of the photocatalyst [66, 67].

4. Conclusion

In conclusion, the photocatalytic performance, crystal structure and charge transfer properties of the photocatalyst are depend on the synthesis method. The synthesis method is divided into 6 ways and each method has specific advantage side. The photocatalytic semiconductors highly used for the photocatalytic reduction of CO₂. Principle side of photocatalytic CO₂ reduction like thermodynamics, mass transfer, and selectivity and reaction mechanism have been deliberated. The mechanism of enhancement of photocatalysis by graphene: semiconductors possess a low-energy VB which has a full of electrons, a high-energy CB which has an empty orbital and has a bandgap difference between two band state. The yield and efficiency of process have been significantly

refined by recent efforts particularly through multinary and functionalized photocatalysts. The efficiency of the photocatalytic reaction depends greatly on the efficiency of electron transfer and charge transfer from metal/metal oxide to graphene (carbon material). On the other hand, the photocatalytic carbon dioxide (CO₂) reduction in aqueous media provides a potential and convenient way for fulfilling increasing fossil energy demand and relieving global warming problems. In conclusion, the combination of semiconductor with graphene, the charge transfer properties, bandgap, the recombination coefficient and the condition of reduction process are the main factors for the photocatalytic reduction of carbon dioxide.

Reference

1. M. Tahir, N.S. Amin, Advances in visible light responsive titanium oxide-based photocatalysts for CO₂ conversion to hydrocarbon fuels, *Energy Convers Manage*, 76 (2013), pp. 194-214
2. Y. Xia, J.Y. Reaction, rational design of highly active photocatalysts for CO₂ conversion, *Chem*, 6 (2020), pp. 1039-1040
3. X.-D. Wang, Y.-H. Huang, J.-F. Liao, Y. Jiang, L. Zhou, X.-Y. Zhang, *et al.*, In situ construction of a Cs₂SnI₆ perovskite nanocrystal/SnS₂ nanosheet heterojunction with boosted Interfacial charge transfer, *J Am Chem Soc*, 141 (2019), pp. 13434-13441
4. P. Zhou, X. Wang, S. Yan, Z. Zou, Solid solution photocatalyst with spontaneous polarization exhibiting low recombination toward efficient CO₂ photoreduction, *ChemSusChem*, 9 (2016), pp. 2064-2068
5. F. Chu, S. Li, H. Chen, L. Yang, O. Ola, M. Maroto-Valer, *et al.*, Modeling photocatalytic conversion of carbon dioxide in bubbling twin reactor, *Energy Convers Manage*, 149 (2017), pp. 514-525
6. K. Yuan, L. Yang, X. Du, Y. Yang, Performance analysis of photocatalytic CO₂ reduction in optical fiber monolith reactor with multiple inverse lights, *Energy Convers Manage*, 81 (2014), pp. 98-105
7. X. Huang, Q. Shen, J. Liu, N. Yang, G. Zhao, A CO₂ adsorption-enhanced semiconductor/metal-complex hybrid photoelectrocatalytic interface for efficient formate production, *Energy Environ Sci*, 9 (2016), pp. 3161-3171
8. J. Wu, Y. Huang, W. Ye, Y. Li, CO₂ reduction: from the electrochemical to photochemical approach, *Adv Sci (Weinh)*, 4 (2017), pp. 1700194
9. W. van Roosbroeck, W. Shockley, Photon-radiative recombination of electrons and holes in Germanium, *Phys Rev*, 94 (1954), pp. 1558-1560
10. R. Hall, Recombination processes in semiconductors, *Proc IEE-Part B: Electron Commun Eng*, 106 (1959), pp. 923-931
11. S. Feng, X. Chen, Y. Zhou, W. Tu, P. Li, H. Li, *et al.*, Na₂V₆O₁₆ · xH₂O nanoribbons: large-scale synthesis and visible-light photocatalytic activity of CO₂ into solar fuels, *Nanoscale*, 6 (2014), pp. 1896-1900
12. B. Qin, Y. Li, H. Wang, G. Yang, Y. Cao, H. Yu, *et al.*, Efficient electrochemical reduction of CO₂ into CO promoted by sulfur vacancies, *Nano Energy*, 60 (2019), pp. 43-51
13. H. Wang, L. Zhang, K. Wang, X. Sun, W. Wang, Enhanced photocatalytic CO₂ reduction to methane over WO₃ · 0.33H₂O via Mo doping, *Appl Catal B*, 243 (2019), pp. 771-779
14. J. Albo, M. Alvarez-Guerra, P. Castaño, A. Irabien, Towards the electrochemical conversion of carbon dioxide into methanol, *Green Chem*, 17 (2015), pp. 2304-2324
15. M. Subrahmanyam, S. Kaneco, N. Alonso-Vante, A screening for the photo reduction of carbon dioxide supported on metal oxide catalysts for C1-C3 selectivity, *Appl Catal B*, 23 (1999), pp. 169-174
16. N. Sasirekha, S.J.S. Basha, K. Shanthi, Photocatalytic performance of Ru doped anatase mounted on silica for reduction of carbon dioxide, *Appl Catal B*, 62 (2006), pp. 169-180
17. E. Karamian, S. Sharifnia, On the general mechanism of photocatalytic reduction of CO₂, *Journal of*

- CO₂ Utilization, 16 (2016), pp. 194-203
18. J.-Y. Liu, X.-Q. Gong, A.N. Alexandria, Mechanism of CO₂ photocatalytic reduction to methane and methanol on defected anatase TiO₂ (101): a density functional theory study, *The Journal of Physical Chemistry C*, 123 (2019), pp. 3505-3511
 19. R. Crovetto, Evaluation of solubility data of the system CO₂-H₂O from 273 K to the critical point of water, *J Phys Chem Ref Data*, 20 (1991), pp. 575-589
 20. X. Li, H. Liu, D. Luo, J. Li, Y. Huang, H. Li, *et al.*, Adsorption of CO₂ on heterostructure CdS(Bi₂S₃)/TiO₂ nanotube photocatalysts and their photocatalytic activities in the reduction of CO₂ to methanol under visible light irradiation, *Chem Eng J*, 180 (2012), pp. 151-158.
 21. O. Zambaga., Y.C. Kwang., W.C. Oh. Novel Micro and Nanostructure of AgCuInS₂-Graphene-TiO₂ Ternary Composite for Photocatalytic CO₂ Reduction for Methanol Fuel, *ACS Omega*, 5 (2020), pp. 26389-26401.
 22. Y. Chen, Q. Tang, Z. Ye, Y. Li, Y. Yang, H. Pu, G. Li. Monolithic Zn_xCe_{1-x}O₂ catalysts for catalytic synthesis of dimethyl carbonate from CO₂ and methanol. *New, J. Chem*, 44 (2020) , pp, 12522-12530.
 23. F.L. Li, H. J. Zhang, Synthesis of hollow sphere and 1D structural materials by sol-gel process, *Materials*, 10 (2017), pp. 995-1012.
 24. Q. Hu, Y. Li, N. Zhao, C. Ning, X. Chen, Facile synthesis of hollow mesoporous bioactive glass sub-micron spheres with a tunable cavity size, *Mater. Lett.*, 134 (2014), pp. 130-133
 25. X.-Y. Yang, L.-H. Chen, Y. Li, J.C. Rooke, C. Sanchez, B.-L. Su, Hierarchically porous materials: synthesis strategies and structure design, *Chem. Soc. Rev.*, 46 (2017), pp. 481-558
 26. Y. Li, J. Shi, Hollow-structured mesoporous materials: chemical synthesis, functionalization and applications, *Adv. Mater.*, 26 (2014), pp. 3176-3205
 27. J. Sun, G. Chen, J. Wu, H. Dong, G. Xiong, Bismuth vanadate hollow spheres: Bubble template synthesis and enhanced photocatalytic properties for photodegradation, *Appl. Catal. B: Environ.*, 132 (2013), pp. 304-314.
 28. J. Sun, G. Chen, J. Wu, H. Dong, G. Xiong, Xiong, Bismuth vanadate hollow spheres: Bubble template synthesis and enhanced photocatalytic properties for photodegradation, *Appl. Catal. B: Environ.*, 132 (2013), pp. 304-314.
 29. Y. Li, J. Liu, X. Huang, G. Li, Hydrothermal synthesis of Bi₂WO₆ uniform hierarchical microspheres, *Cryst. Growth Des.*, 7 (2007), pp. 1350-1355
 30. R. Buonsanti, V. Grillo, E. Carlino, C. Giannini, T. Kipp, R. Cingolani, P.D. Cozzoli, Nonhydrolytic synthesis of high-quality anisotropically shaped brookite TiO₂ nanocrystals, *J. Am. Chem. Soc.*, 130 (2008), pp. 11223-11233
 31. J. Yu, C.-Y. Xu, F.-X. Ma, S.-P. Hu, Y.-W. Zhang, L. Zhen, Monodisperse SnS₂ nanosheets for high-performance photocatalytic hydrogen generation, *ACS Appl. Mater. Interfaces*, 6 (2014), pp. 22370-22377.
 32. J. Yu, C.-Y. Xu, F.-X. Ma, S.-P. Hu, Y.-W. Zhang, L. Zhen, Monodisperse SnS₂ nanosheets for high-performance photocatalytic hydrogen generation, *ACS Appl. Mater. Interfaces*, 6 (2014), pp. 22370-22377.
 33. H. Yang, X.-L. Wu, M.-H. Cao, Y.-G. Guo, Solvothermal synthesis of LiFePO₄ hierarchically dumbbell-like microstructures by nanoplate self-assembly and their application as a cathode material in lithium-ion batteries, *J. Phys. Chem. C*, 113 (2009), pp. 3345-3351
 34. X.K. Wang, C. Wang, W.Q. Jiang, W.-L. Guo, J.-G. Wang, Sonochemical synthesis and characterization of Cl-doped TiO₂ and its application in the photodegradation of phthalate ester under visible light irradiation, *Chem. Eng. J.*, 189 (2012), pp. 288-294
 35. J. Fu, G.Z. Kyzas, Z. Cai, E.A. Deliyanni, W. Liu, D. Zhao, Photocatalytic degradation of phenanthrene by graphite oxide-TiO₂-Sr(OH)₂/SrCO₃ nanocomposite under solar irradiation: effects of water quality

- parameters and predictive modeling, *Chem. Eng. J.*, 335 (2018), pp. 290-300
36. J. Jiang, Q. Zhang, X. Zhan, F. Chen, A multifunctional gelatin-based aerogel with superior pollutants adsorption, oil/water separation and photocatalytic properties, *Chem. Eng. J.*, 358 (2019), pp. 1539-1551
 37. M. Li, C. Bian, G. Yang, X. Qiang, Facile fabrication of water-based and non-fluorinated superhydrophobic sponge for efficient separation of immiscible oil/water mixture and water-in-oil emulsion, *Chem. Eng. J.*, 368 (2019), pp. 350-358
 38. T. Razpotnik, J. Macek, Synthesis of nickel oxide/zirconia powders via a modified Pechini method, *J. Eur. Ceram. Soc.* 27 (2007) 1405-1410.
 39. M.P. Pechini, Method of Preparing Lead and Alkaline-Earth Titanates and Niobates and Coating Method Using the Same to Form a Capacitor-US PAT., 3.330.697, 1967.
 40. Zambaga Otgonbayar, Kwang Youn Cho, Won Chun Oh, Enhanced photocatalytic activity of CO₂ reduction to methanol through the use of a novel-structured CuCaAg₂Se-graphene-TiO₂ ternary nanocomposite, *New, J. Chem.*, (2020).
 41. H. Zhao, F. Pan, Y. Li, A review on the effects of TiO₂ surface point defects on CO₂ photoreduction with H₂O, *J. Mater.*, 3 (2017), pp. 17-32
 42. D. Chen, L. Zou, S. Li, F. Zheng, Nano spherical like reduced graphene oxide decorated TiO₂ nanoparticles: an advanced catalyst for the hydrogen evolution reaction, *Sci. Rep.*, 6 (2016), p. 20335
 43. M.P. Kumar, T. Kesavan, G. Kalita, P. Ragupathy, T.N. Narayanan, D.K. Pattanayak, On the large capacitance of nitrogen doped graphene derived by a facile route, *RSC Adv.*, 4 (2014), pp. 38689-38697
 44. S. Indrawirawan, H. Sun, X. Duan, S. Wang, Low temperature combustion synthesis of nitrogen-doped graphene for metal-free catalytic oxidation, *J. Mater. Chem. A.*, 3 (2015), pp. 3432-3440
 45. L.A. Gu, J.Y. Wang, H. Cheng, Y.Z. Zhao, L.F. Liu, X.J. Han, One-step preparation of graphene-supported anatase TiO₂ with exposed {001} facets and mechanism of enhanced photocatalytic properties, *ACS Appl. Mater. Interfaces*, 5 (2013), pp. 3085-3093
 46. Joshua O. Olowoyo, Manoj Kumar, Bhupender Singh, Vincent O. Oninla, Jonathan O. Babalola, Héctor Valdés, Alexander V. Vorontsov, Umesh Kumar, Self-assembled reduced graphene oxide-TiO₂ nanocomposites: Synthesis, DFTB+ calculations, and enhanced photocatalytic reduction of CO₂ to methanol, *Carbon*, 147 (2019) 385-397.
 47. S. Sorcar, Y. Hwang, C.A. Grimes, S.-I. In, Highly enhanced and stable activity of defect-induced titania nanoparticles for solar light-driven CO₂ reduction into CH₄, *Mater. Today.*, 20 (2017), pp. 507-515
 48. S. Sorcar, J. Thompson, Y. Hwang, Y.H. Park, T. Majima, C.A. Grimes, J.R. Durrant, S.-I. In, High-rate solar-light photoconversion of CO₂ to fuel: controllable transformation from C₁ to C₂ products, *Energy Environ. Sci.*, 11 (2018), pp. 3183-3193
 49. G. Lui, J.-Y. Liao, A. Duan, Z. Zhang, M. Fowler, A. Yu, Graphene-wrapped hierarchical TiO₂ nanoflower composites with enhanced photocatalytic performance, *J. Mater. Chem. A*, 1 (2013), pp. 12255-12262
 50. C. Zhou, S. Wang, Z. Zhao, Z. Shi, S. Yan, Z. Zou, A Facet-Dependent Schottky-Junction Electron Shuttle in a BiVO₄{010}-Au-Cu₂O Z-Scheme Photocatalyst for Efficient Charge Separation, *Adv. Funct. Mater.*, 28 (2018), p. 1801214
 51. R. Jaiswal, J. Bharambe, N. Patel, A. Dashora, D.C. Kothari, A. Miotello, Copper and nitrogen co-doped TiO₂ photocatalyst with enhanced optical absorption and catalytic activity, *Appl. Catal., B*, 168 (2015), pp. 333-341
 52. D.J. Chen, L.L. Zou, S.X. Li, F.Y. Zheng, Nanospherical like reduced graphene oxide decorated TiO₂ nanoparticles: an advanced catalyst for the hydrogen evolution reaction, *Sci. Rep.*, 6 (2016), p. 20335
 53. W.L. Wang, Z.F. Wang, J.J. Liu, Z. Luo, S.L. Sui, *et al.*, Single-step one-pot synthesis of TiO₂ nanosheets

- doped with sulfur on reduced graphene oxide with enhanced photocatalytic activity, *Sci. Rep.*, 7 (2017), pp. 46610
54. Y.Y. Zhang, X.G. Hou, T.T. Sun, X.L. Zhao, Calcination of reduced graphene oxide decorated TiO₂ composites for recovery and reuse in photocatalytic applications, *Ceram. Int.*, 43 (2017), pp. 1150-1159
 55. W.Q. Fan, Q.H. Lai, Q.H. Zhang, Y. Wang, Nanocomposites of TiO₂ and reduced graphene oxide as efficient photocatalysts for hydrogen evolution, *J. Phys. Chem. C*, 115 (2011), pp. 10694-10701
 56. Y.J. Li, L.Y. Li, C.W. Li, W. Chen, M.X. Zeng, Carbon nanotube/titania composites prepared by a micro-emulsion method exhibiting improved photocatalytic activity, *Appl. Catal., A*, 427 (2012), pp. 1-7
 57. X. Li, Y. Sun, J. Xu, Y. Shao, J. Wu, X. Xu, Y. Pan, H. Ju, J. Zhu, Y. Xie, Selective visible-light-driven photocatalytic CO₂ reduction to CH₄ mediated by atomically thin CuIn₅S₈ layers, *Nat. Energy*, 4 (2019), pp. 690-699
 58. S.R. Lingampalli, M.M. Ayyub, C.N.R. Rao, Recent progress in the photocatalytic reduction of carbon dioxide, *ACS Omega*, 2 (2017), pp. 2740-2748
 59. L.-Y. Lin, Y. Nie, S. Kavadiya, T. Soundappan, P. Biswas, N-doped reduced graphene oxide promoted nano TiO₂ as a bifunctional adsorbent/photocatalyst for CO₂ photoreduction: Effect of N species, *Chem. Eng. J.*, 316 (2017), pp. 449-460
 60. W.-N. Wang, J. Park, P. Biswas, Rapid synthesis of nanostructured Cu-TiO₂-SiO₂ composites for CO₂ photoreduction by evaporation driven self-assembly, *Catal. Sci. Technol.*, 1 (2011), pp. 593-600
 61. L. Spadaro, F. Arena, A. Palella, Which future route in the methanol synthesis? Photocatalytic reduction of CO₂, the new challenge in the solar energy exploitation, in: *Methanol*, Elsevier (2018) 429-472.
 62. S. Xie, Y. Wang, Q. Zhang, W. Deng, Y. Wang, MgO-and Pt-promoted TiO₂ as an efficient photocatalyst for the preferential reduction of carbon dioxide in the presence of water, *ACS Catal.*, 4 (2014), pp. 3644-3653.
 63. Z. Zhang, Y. Liang, H. Huang, X. Liu, Q. Li, L. Chen, D. Xu, *Angew. Chem. Int. Ed.*, 58 (2019), pp. 7263-7267
 64. Yingying Wang, Anlin Huang, Zhenzhen Zhang, Cong Wang, Yuying Yang, Qi Li, Dongsheng Xu, Lead-free perovskite Cs₂AgBiBr₆@g-C₃N₄ Z-scheme system for improving CH₄ production in photocatalytic CO₂ reduction, *Applied Catalysis B: Environmental*, 282 (2021), 119570.
 65. Joshua O. Olowoyo, Manoj Kumar, Bhupender Singh, Vincent O. Oninla, Jonathan O. Babalola, Héctor Valdés, Alexander V. Vorontsov, Umesh Kumar, Self-assembled reduced graphene oxide-TiO₂ nanocomposites: Synthesis, DFTB+ calculations, and enhanced photocatalytic reduction of CO₂ to methanol, *Carbon*, 147 (2019) 385-397
 66. Chaitanya B. Hiragond, Junho Lee, Hwapyong Kim, Jin-Woo Jung, Chang-Hee Cho, Su-Il In, A novel N-doped graphene oxide enfolded reduced titania for highly stable and selective gas-phase photocatalytic CO₂ reduction into CH₄: An in-depth study on the interfacial charge transfer mechanism, *Chem. Eng. J.*, (2020), pp. 127978.
 67. F. Liu, K. Huang, S. Ding, S. Dai, One-step synthesis of nitrogen-doped graphene-like meso-macroporous carbons as highly efficient and selective adsorbents for CO₂ capture, *J. Mater. Chem. A*, 4 (2016), pp. 14567-14571.



This document was created with the Win2PDF "print to PDF" printer available at <http://www.win2pdf.com>

This version of Win2PDF 10 is for evaluation and non-commercial use only.

This page will not be added after purchasing Win2PDF.

<http://www.win2pdf.com/purchase/>